crystals

MDPI

Article

O-Vacancy-Rich ε-MnO_2 Synthesized at Hydrophobic Interface: An Efficient Fenton-like Catalyst for Removing Ciprofloxacin from Water

Yulong Chen †, Yuan Chi †, Xiao Wu *, Cong Lin, Tengfei Lin, Min Gao, Chunlin Zhao and Baisheng Sa *

College of Materials Science and Engineering, Fuzhou University, Fuzhou 350108, China; ylchen@fzu.edu.cn (Y.C.); n191820051@fzu.edu.cn (Y.C.); lincong@fzu.edu.cn (C.L.); tflin@fzu.edu.cn (T.L.); gaom@fzu.edu.cn (M.G.); zhaochunlin@fzu.edu.cn (C.Z.)

* Correspondence: wuxiao@fzu.edu.cn (X.W.); bssa@fzu.edu.cn (B.S.)

† These authors contributed equally to the work.

Abstract: The widespread use of pharmaceuticals and personal care products (PPCPs) in many fields has brought convenience to human lives but has also caused unavoidable environmental pollution issues. In particular, the resistance gene problem resulting from accumulating antibiotics that cannot be fully absorbed by biological individuals has been a concern; thus, it is urgent to find efficient technologies to boost the degradation efficiency of antibiotics in the environment. Here, an ε-MnO_2 catalyst was prepared by a novel droplet-interface-drying method and utilized as a Fenton-like catalyst for efficiently degrading ciprofloxacin (CIP). The ε-MnO_2 shell was formed preferentially at the gas–liquid interface and then continued to decompose into ε-MnO_2 with abundant O vacancies in the air-insulated microcavity. The XPS result confirms that this particular preparation method can regulate the content of O vacancies in the material. Compared with ε-MnO_2 samples obtained by the direct drying method (ε-MnO_2-B), the catalytic performance of ε-MnO_2 prepared by the droplet-interface-drying method (ε-MnO_2-P) is significantly improved. By activating peroxymonosulfate (PMS) with the ε-MnO_2-P catalyst, the CIP degradation efficiency can reach 84.1%. The detection and analysis of reactive oxygen species (ROS) in the ε-MnO_2-P/PMS oxidation system confirms that ·OH, $SO_4^{\cdot -}$ and $^1O_2$ are the main ROS for CIP degradation. This study highlights the creation of miniature hypoxic space to regulate the content of O vacancies in ε-MnO_2, providing a new idea for the synthesis of other O-vacancy-rich materials.

Keywords: droplet-interface-drying method; Fenton-like oxidation; ε-MnO_2; ciprofloxacin; water purification

Citation: Chen, Y.; Chi, Y.; Wu, X.; Lin, C.; Lin, T.; Gao, M.; Zhao, C.; Sa, B. O-Vacancy-Rich ε-MnO_2 Synthesized at Hydrophobic Interface: An Efficient Fenton-like Catalyst for Removing Ciprofloxacin from Water. *Crystals* **2023**, *13*, 1664. https://doi.org/10.3390/cryst13121664

Academic Editor: Yael Diskin-Posner

Received: 17 November 2023
Revised: 30 November 2023
Accepted: 3 December 2023
Published: 6 December 2023

1. Introduction

The rising living standard of people has led to an increasing focus on health issues, so the usage of pharmaceuticals and personal care products (PPCPs) is increasing year by year. The pollution of the water environment caused by the resulting organic residues began to attract the attention of numerous experts [1,2]. Antibiotics are widely used in various fields because of their excellent antibacterial performance. Ciprofloxacin (CIP), as a broad-spectrum antibiotic, is used in large quantities, but it is difficult for it to be fully absorbed by humans or animals and it is degraded with traditional wastewater treatment methods [3]. CIP tends to accumulate in the natural environment with sewage, resulting in unavoidable biotoxicity that harms humans and other organisms, even with low levels of CIP [4–6]. In the worst-case scenario, antibiotic-resistant bacteria (ARB) along with antibiotic resistance genes (ARGs) are produced and spread in the water column. Therefore, a simple and efficient wastewater treatment technology to remove CIP residue from the effluent is urgently needed.

Advanced oxidation processes (AOPs) are commonly used sewage treatment technologies that mainly rely on the activation of H_2O_2 or peroxymonosulfate (PMS) to generate different radicals (e.g., hydroxyl radicals (·OH) and sulphate radicals ($SO_4^{\cdot -}$)) to degrade organic pollutants to purify water [7,8]. In addition, compared to ·OH, $SO_4^{\cdot -}$ has caused extensive concern on account of its higher redox potential (E_0 = 2.8~3.1 eV), wider pH range and lower cost [9–11]. Therefore, the production of reactive oxygen species (ROS) by activating PMS is very promising and is also known as sulphate radical-based advanced oxidation processes (SR-AOPs).

There are many studies using various methods to activate PMS, such as transition metal catalysts [12], UV light irradiation [13], and heating [14]. Therein, transition metal catalysts have been widely studied because of the presence of metal centres, which can provide more catalytically active sites, and the reaction conditions are mild and convenient [15,16]. Cobalt (Co) is considered to be one of the most efficient transition metals for the activation of PMS, but its practical use has yet to be explored due to shortcomings such as toxicity and a tendency to cause secondary contamination [17,18]. Equally, the adjacent metal manganese (Mn) has been widely used in AOPs due to its low cost, abundance in nature and relatively low toxicity. Many studies have illustrated and explained the effectiveness of different manganese oxides for activating PMS, such as α-, β-, and γ-MnO_2 [19], Mn_2O_3 [20] and Mn_3O_4 [21]. These results indicate that the different crystalline manganese oxides have various degradation effects on pollutants.

As is known to all, the structural defects of catalyst materials display a positive effect on catalytic performance. ε-MnO_2 is a promising Fenton-like catalyst material because it has more abundant defects and higher disorder than other crystalline manganese oxides. Its internal structure is a disordered cross-combination of pyrolusite structure (1 × 1 tunnel) and rhombohedral manganese structure (1 × 2 tunnel). This special highly disordered structure makes ε-MnO_2 a prospective catalyst material [22–24]. In this work, a very simple method was used, and two kinds of ε-MnO_2 samples were obtained by varying the reaction interface. Both samples were used as Fenton-like catalysts for the removal of CIP from water, and the adsorption capacity of CIP and activation performance of PMS were assessed by UV spectroscopy. The influence of factors such as the initial pH value of solution and catalysts or the PMS dosage on the CIP removal efficiency were also investigated. In addition, the main ROS in the ε-MnO_2/PMS oxidation system, the stability of the ε-MnO_2 catalyst and the removal mechanism of CIP were also systematically demonstrated. This study displays a simple and special fabrication method of ε-MnO_2, which provides a novel design strategy for the preparation of efficient SR-AOP catalysts.

2. Experimental Procedure

2.1. Materials and Chemicals

Barium chlorate monohydrate ($Ba(ClO_3)_2{\cdot}H_2O$) was purchased from Advanced Technology & Industrial Co., Ltd (Hong Kong, China). Manganese sulphate ($MnSO_4{\cdot}H_2O$), potassium monopersulate triple salt (PMS, $KHSO_5{\cdot}0.5KHSO_4{\cdot}0.5K_2SO_4$), 5,5-dimethyl-1-pyrroline N-oxide (DMPO), 2,2,6,6-tetramethylpiperidine (TEMP), tert-butanol (TBA) and ciprofloxacin hydrochloride (CIP) were purchased from Shanghai Aladdin Biochemical Co., Ltd. (Shanghai, China). Hydrochloric acid (HCl) was obtained from Fujian Chemical Glass Scientific and Educational Instrument Co., Ltd. (Fuzhou, China). Sodium hydroxide (NaOH) was purchased from Sinopharm Chemical Reagent Co., Ltd. (Shanghai, China). Isopropyl alcohol (IPA) was obtained from Shanghai Titan Technology Co., Ltd. (Shanghai, China). All reagents were directly used without further purification. In addition, deionized water (DI) was used as experimental water in all procedures.

2.2. Synthesis of ε-MnO_2 Catalysts

A total of 13.42 g $Ba(ClO_3)_2{\cdot}H_2O$ was dissolved in DI water (50 mL), and 7.72 g $MnSO_4{\cdot}H_2O$ was dissolved in 30 mL DI water. Then, the above two solutions were mixed and stirred to obtain a uniform suspension after 10 min. Soon afterwards, the

mixture was centrifuged at 8000 r/min to obtain a $Mn(ClO_3)_2$ solution. A similar synthetic process of $Mn(ClO_3)_2$ solution has been recorded in previous literature [22]. The prepared solution was sealed and stored under refrigeration away from light and used for subsequent experiments. A certain amount of $Mn(ClO_3)_2$ solution was subsequently dried with a hydrophilic interface to obtain ε-MnO_2-B powders (in a beaker), or with a hydrophobic interface to acquire ε-MnO_2-P powders (on a PTFE plate). Then, the products were ground, washed and stored in sealed containers.

2.3. Characterizations

The surface morphology of the ε-MnO_2 samples was observed by a field emission scanning electron microscope (FESEM, SUPRA 55, Carl Zeiss, Jena, Germany). Transmission electron microscopy images were obtained through a transmission electron microscope (TEM, F200i, FEI, Hillsboro, OR, USA). The crystalline phases of the materials were measured with powder X-ray diffraction (XRD, ULTIMA III, Rigaku, Tokyo, Japan) using a Cu Kα target. The chemical states of Mn and O were analysed by X-ray photoelectron spectrometry (XPS, K-Alpha+, Thermo Fisher Scientific, Waltham, MA, USA). N_2 adsorption–desorption isotherms and specific surface area measurements were performed using an adsorption apparatus (BET, 2460, Micromeritics Instrument, Norcross, GA, USA). Raman spectra were characterized with a spectrometer (Raman, DXR2xi, Thermo Fisher Scientific, USA) with an excitation wavelength of 532 nm.

2.4. Degradation Procedure and Analytical Methods

To investigate the PMS activation ability of the prepared ε-MnO_2, batch experiments were carried out with a shaker at 240 rpm. For the typical experiment, 0.2 g/L catalysts were added into the CIP solution. Before the reaction started, adsorption–desorption equilibrium was reached by shaking for 60 min. The Fenton-like reaction was triggered after instilling 1 mM PMS. The initial pH was adjusted by 0.1 M HCl and NaOH. After reaching a predetermined time, 10 mL of CIP was filtered through a membrane (with a pore size of 0.22 μm) to remove the catalyst powder, which was then immediately detected using a Metash UV-6000 spectrophotometer. To explore the ROS in the reaction, the contribution of different ROS to the reaction was confirmed by UV–vis analysis after bursting of ·OH and $SO_4^{\cdot -}$ by adding IPA and TBA to the solution. To further bear out the ROS, DMPO and TEMP were added to capture different ROS, and their signals were detected by Bruker EMXnano electron paramagnetic resonance (EPR).

3. Results and Discussion

The surface morphology and grain sizes of the ε-MnO_2-P and ε-MnO_2-B samples were observed by both SEM and TEM images. As can be seen in Figure 1a, ε-MnO_2-B exhibits non-uniform spherical grains on the micron scale with severe agglomeration. Figure 1b displays the enlarged image, and the spherical particles are composed of numerous tiny interwoven burrs exhibiting a porous structure. The micromorphology of ε-MnO_2-B was further observed by TEM, and, from Figure 1c, it can be clearly observed that the burrs on the surface of ε-MnO_2-B are formed by closely interwoven and stacked rod-like particles, which is consistent with the SEM result. Compared to ε-MnO_2-B, the ε-MnO_2-P sample demonstrates completely different morphological characteristics. As seen in Figure 1d,e, the ε-MnO_2-P particles present an irregular nanospherical morphology, which is obviously smaller than that of ε-MnO_2-B particles. The TEM image (Figure 1f) reveals that ε-MnO_2-P is composed of nanorods and nanoparticles. The results demonstrate that ε-MnO_2-B generated by direct heating decomposition at the hydrophilic interface easily forms large spherical particles, and the surface of the particles is composed of a rod-like interlocking burr structure. However, the large particles with severe agglomeration are not conducive to the activation reaction of the catalyst. While the droplet drying method designed at the hydrophobic interface is propitious to forming a cavity shell at the gas–liquid interface, the subsequent decomposition reaction can be carried out in a microcavity that is isolated from

air. As a consequence, ε-MnO_2-P nanoparticles with completely different morphologies were obtained. This method opens up a new route for the preparation of nanomaterials in the future. In addition, the agglomeration phenomena of ε-MnO_2-B and ε-MnO_2-P particles were serious and inevitable, so the samples were subjected to ultrasonic treatment for 30 s before subsequent degradation experiments.

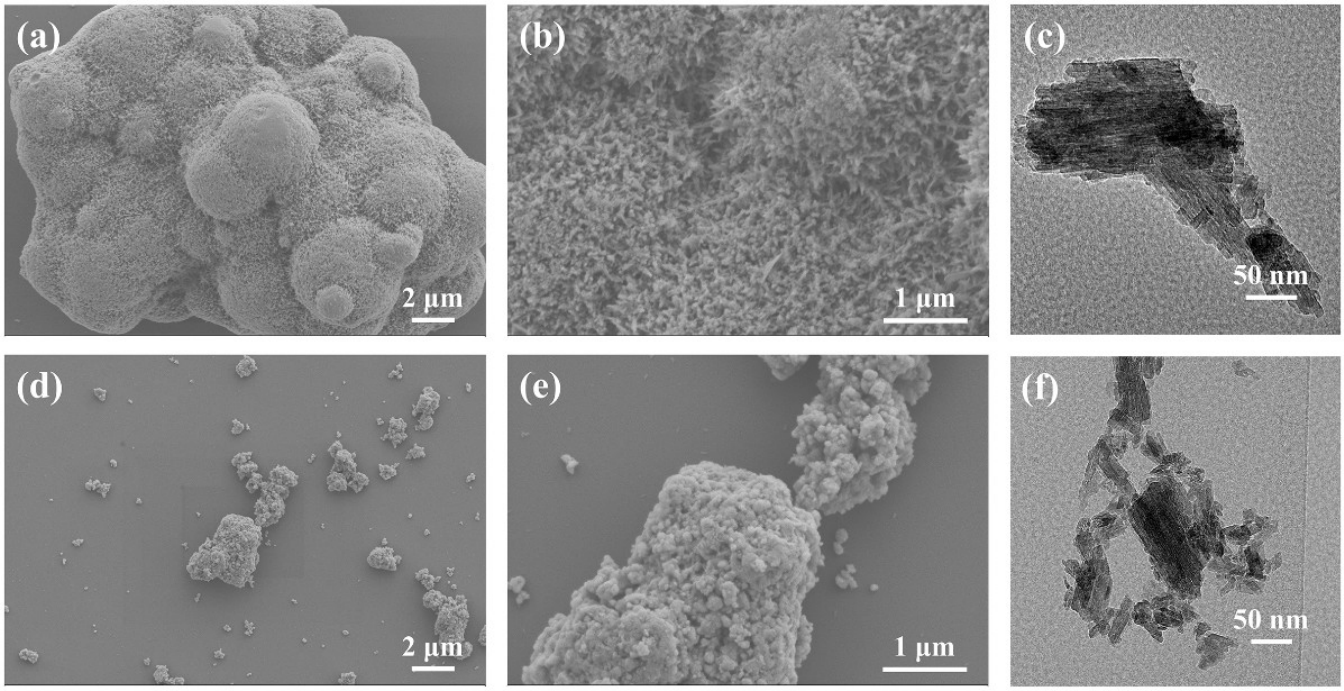

Figure 1. SEM images of ε-MnO_2-B (**a**,**b**) and ε-MnO_2-P (**d**,**e**); TEM images of ε-MnO_2-B (**c**) and ε-MnO_2-P (**f**).

The crystal structures of ε-MnO_2-B and ε-MnO_2-P before and after CIP removal were analysed by means of XRD. As depicted in Figure 2a, the XRD patterns of both ε-MnO_2-B and ε-MnO_2-P are found to be in agreement by comparison with the standard card of ε-MnO_2 (JCPDS No. 30-0820). The characteristic peaks at 21.0°, 37.1°, 42.4°, 56.0° and 66.8° correspond to the (001), (100), (101), (102) and (110) crystalline planes of ε-MnO_2, respectively. There are no extra peaks present in the XRD pattern of ε-MnO_2-P after the oxidation reaction. This indicates that the crystalline phase structure of ε-MnO_2-P did not change either before or after the reaction, proving that the prepared ε-MnO_2-P displayed relatively good chemical stability. Moreover, ε-MnO_2-B has higher crystallinity than ε-MnO_2-P, and materials with lower crystallinity usually have more active sites, e.g., oxygen vacancies [25]. The presence of oxygen vacancies can reduce the charge transfer resistance and then enhance the charge transfer rate, thus accelerating the mobility of electrons, which ultimately affects the result of Fenton-like reactions [25,26].

The adsorption performance of the catalyst is also an important indicator for the Fenton-like oxidation process, and the specific surface area and pore distribution of the catalyst are closely related to the adsorption capacity. The adsorption performance of both ε-MnO_2-P and ε-MnO_2-B can be obtained by analysing the nitrogen adsorption and desorption isotherm curves. As shown in Figure 2b, the occurrence times of adsorption and desorption are different within the range of relative pressures of 0.4 and 1, and ε-MnO_2-P and ε-MnO_2-B both exhibit an IV isotherm type with an H3-type hysteresis loop, belonging to a typical mesoporous structure [27,28]. The calculated specific surface areas for ε-MnO_2-P and ε-MnO_2-B are 99.24 m^2/g and 29.84 m^2/g, respectively. The specific surface area of ε-MnO_2-P is 3.3 times larger than that of ε-MnO_2-B, implying that ε-MnO_2-P has a stronger adsorption capacity. As shown in the inset illustration in Figure 2b, the average

pore sizes of ε-MnO_2-P and ε-MnO_2-B are 4.9 and 3.6 nm, respectively. ε-MnO_2-P possesses a relatively higher specific surface area because the closed microcavity space formed at the hydrophobic interface limits the inside grain growth. A higher specific surface area generally endows ε-MnO_2-P with a strong adsorption capacity, making it able to attract more CIP and PMS molecules.

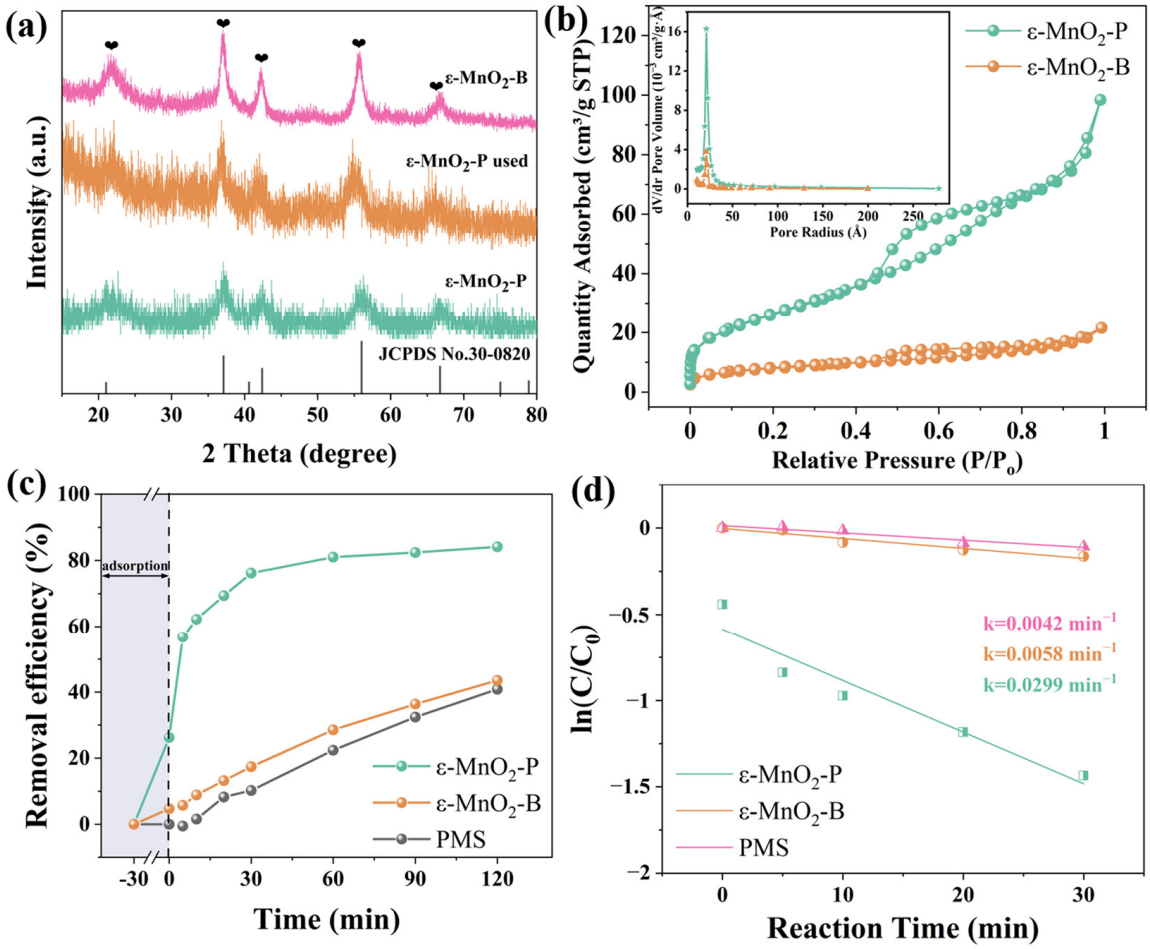

Figure 2. (**a**) XRD patterns of ε-MnO_2-B and ε-MnO_2-P (before and after reaction), (**b**) N_2 adsorption–desorption isotherms of ε-MnO_2-B and ε-MnO_2-P, (**c**) CIP removal efficiency in different oxidation systems, and (**d**) the pseudo-first-order kinetic linear fitting plots. Reaction conditions: [CIP] = 10 ppm, [Catalyst] = 0.2 g/L, [PMS] = 1 mM, without pH adjustment.

The degradation rate of CIP was analysed by UV–Vis spectrophotometry, yielding the results in Figure 2c. After reaching the adsorption–desorption equilibrium, the adsorption of CIP for ε-MnO_2-P can reach 26.2%, while the adsorption capacity of ε-MnO_2-B is only 4.68%, consistent with the results of previous specific surface areas (Figure 2b). After adding 1 mM PMS to initiate the oxidation reaction, the removal efficiency of CIP can reach 84.1% within 120 min, indicating that the prepared ε-MnO_2-P can effectively activate PMS to generate ROS for CIP decomposition. In the system without catalyst, the CIP removal efficiency of pure PMS is 40.8%, which is only slightly higher than the CIP adsorption efficiency of ε-MnO_2-P. Similarly, the CIP removal efficiency of ε-MnO_2-B within 120 min is 43.5%, which is not much different from that of the pure PMS system and much lower than that of ε-MnO_2-P for CIP. And the comparison of catalytic activities for CIP degradation of different ε-MnO_2 is listed in Table 1. The results show that ε-MnO_2-B can hardly adsorb CIP or activate PMS to promote the Fenton-like reaction, probably due to the block structure and serious agglomeration, as well as the small specific surface area and minute quantity of active sites exposed.

Table 1. Comparison of catalytic activities for CIP degradation of ε-MnO_2-P or ε-MnO_2-B by activating PMS.

Sample	Reaction Condition	Adsorption (within 30 min)	Removal Efficiency (within 120 min)
ε-MnO_2-P + PMS	Dried with a hydrophobic interface	26.2%	84.1%
ε-MnO_2-B + PMS	Dried with a hydrophilic interface	4.68%	43.5%

Figure 2d displays the degradation kinetics of CIP in different MnO_2 materials. The rate constant can be calculated by means of the pseudo-first-order kinetic equation $\ln(C/C_0) = -kt$, where C is the CIP concentration at the specified time (mg/L), C_0 is the initial CIP concentration (mg/L), t is the reaction time (min) and k is the rate constant (min^{-1}). According to the above equation, the k values of ε-MnO_2-P, ε-MnO_2-B and PMS are 0.0299, 0.0058 and 0.0042, respectively. The k value of ε-MnO_2-P is 5.2 and 7.1 times higher than that of ε-MnO_2-B and PMS, respectively. This result indicates that ε-MnO_2-P can bring more active sites and adsorb more PMS and CIP molecules, thus activating PMS more efficiently to achieve the desired removal effect. Therefore, ε-MnO_2-P was selected as the main Fenton-like catalyst in the subsequent experiments.

The recyclability measurement of ε-MnO_2-P is displayed in Figure 3a. The removal efficiency of ε-MnO_2-P to CIP remained almost unchanged after the second cycle, while the removal efficiency significantly decreased from 81.8% to 69.1% after the third recycling cycle. This may be because some of the CIP residues covered the ε-MnO_2-P surface after experiencing multiple cycles; thus, the number of exposed active sites reduced. Meanwhile, with the extension of reaction time, the concentration of oxygen vacancies and the valence of Mn altered significantly (which will be verified in the following section), thus weakening the final removal effect.

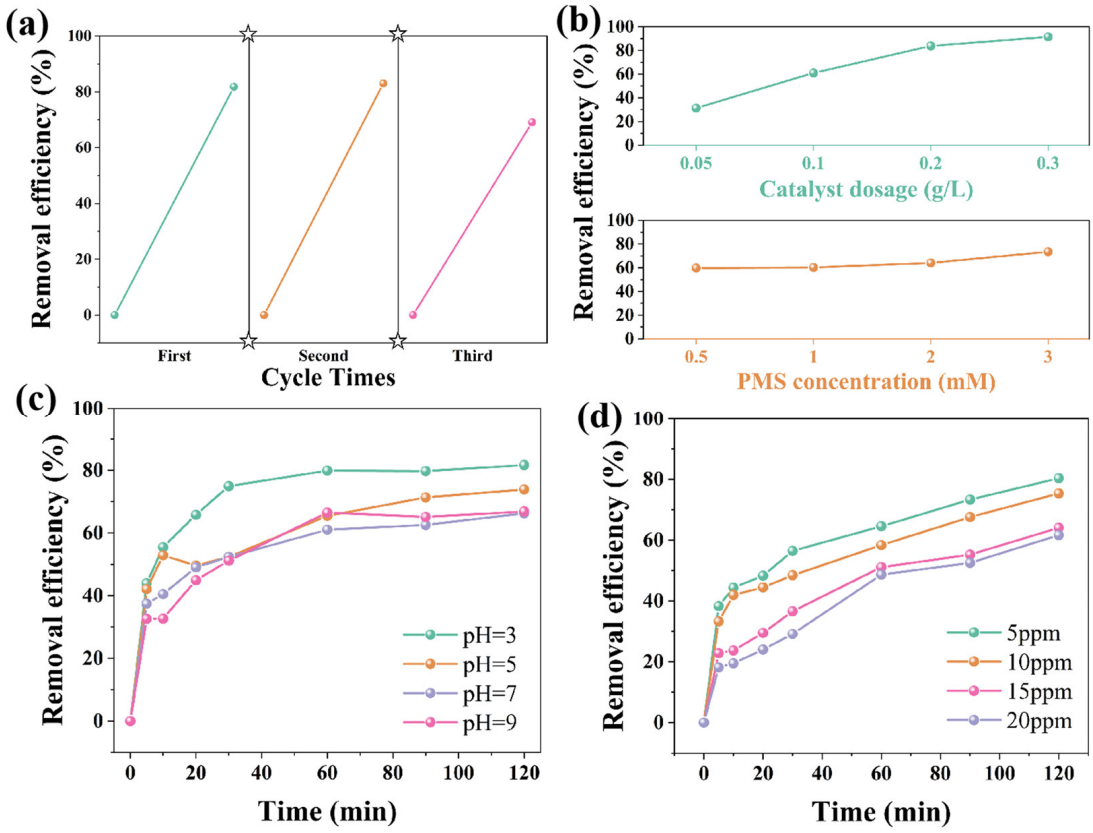

Figure 3. (**a**) Cycling Fenton-like reaction of ε-MnO_2-P. Effects of (**b**) different catalyst dosages and PMS concentrations, (**c**) different initial pH values and (**d**) different initial CIP concentrations.

To further study the influence of different environmental factors on the catalytic performance of ε-MnO_2-P, the effects of different catalyst dosages, PMS concentrations, solution pH values and initial CIP concentrations on the CIP removal efficiency are compared. Figure 3b expresses the impact of catalyst dosage and PMS concentration on CIP removal efficiency. It can be clearly observed that, as the catalyst dosage increases from 0.05 to 0.3 g/L, the removal efficiency of CIP significantly increases, and the maximum removal efficiency reaches 91.5% within 60 min. It is worth noting that the increase in catalyst dosage from 0.2 g/L to 0.3 g/L results in only a slight change in the CIP removal efficiency. This phenomenon should be due to excess active sites not being effectively utilized as the amount of PMS is limited or the agglomeration of active sites occurring at high catalyst concentrations. In addition, increasing the PMS concentration alone can only slightly enhance the removal effect, indicating that a PMS concentration that is too high is not conducive to CIP removal.

The influence of initial pH values (i.e., pH = 3, 5, 7, 9) on CIP removal efficiency is likewise discussed, yielding the results in Figure 3c. Normally, pH value is a key influencer of the free radical pathway ($\cdot OH/SO_4^{\cdot -}$). Consistent with many previous studies, the highest CIP removal efficiency of 81.7% was observed at pH = 3. The degradation rate was slightly higher in acidic environments, probably because the pKa of PMS is 9.4, and when pH < 9.4, the main form of PMS is HSO_5^-, which can react with Mn to generate a Fenton-like reaction. In an alkaline environment, PMS is unstable and easy to react, and HSO_5^- combines with hydroxide ions (OH^-) to form SO_4^{2-} ($2HSO_5^- + 2OH^- \rightarrow 2SO_4^{2-} + O_2 + 2H_2O$). Notably, the CIP removal efficiency of the ε-MnO_2-P/PMS oxidation system also reached over 60% under neutral and alkaline conditions, demonstrating that ε-MnO_2-P can be used in an environment with a wide pH range.

Figure 3d shows the removal performance of the ε-MnO_2-P/PMS system on CIP at different pollutant concentrations. With increasing initial CIP concentrations (from 5, 10, 15 and 20 ppm), the removal efficiency of CIP decreases by 80.3%, 75.3%, 64.1% and 61.6%, respectively. Since the active sites provided by the catalyst for CIP adsorption and PMS activation are limited, PMS is insufficient to remove excessive amounts of contaminants.

XPS measurement was carried out to analyse the elemental composition and corresponding chemical state on the surface of ε-MnO_2. Figure 4a–d show the full and fine spectra of ε-MnO_2-P before and after the reaction. According to the full spectrum presented in Figure 4a, Mn, O and C are mainly present in ε-MnO_2-P whether before or after the reaction, and no obvious impurity peaks can be observed. The change in the chemical states of Mn can usually be obtained from the Mn 3s spectrum (Figure 4b) and the Mn 2p spectrum (Figure 4c). It can be seen from Figure 4b that the spin separation energy (ΔE) of ε-MnO_2-P is 4.96 eV before the reaction and then drops to 4.80 eV after the reaction. On the basis of the equation AOS = 8.956 − 1.126ΔE [23,29], it is easy to calculate that the average oxidation state (AOS) of Mn increases from 3.37 to 3.55, suggesting that the average valence of Mn increased after the reaction. Mn with lower valence participated in the activation reaction of PMS and was oxidized, which ultimately reflected the increase in AOS in the analysis of the XPS results. As depicted in Figure 4c, two main peaks representing Mn^{3+} (641.92 eV) and Mn^{4+} (643.84 eV) can be obtained [30,31]. Before the reaction, the proportions of Mn^{3+} and Mn^{4+} are 69.9% and 30.1%, respectively. After the reaction, the proportion of Mn^{3+} decreases and that of Mn^{4+} increases. This result is consistent with the Mn 3s spectrum, further indicating that Mn^{3+} was consumed more rapidly and played a major role in the reaction.

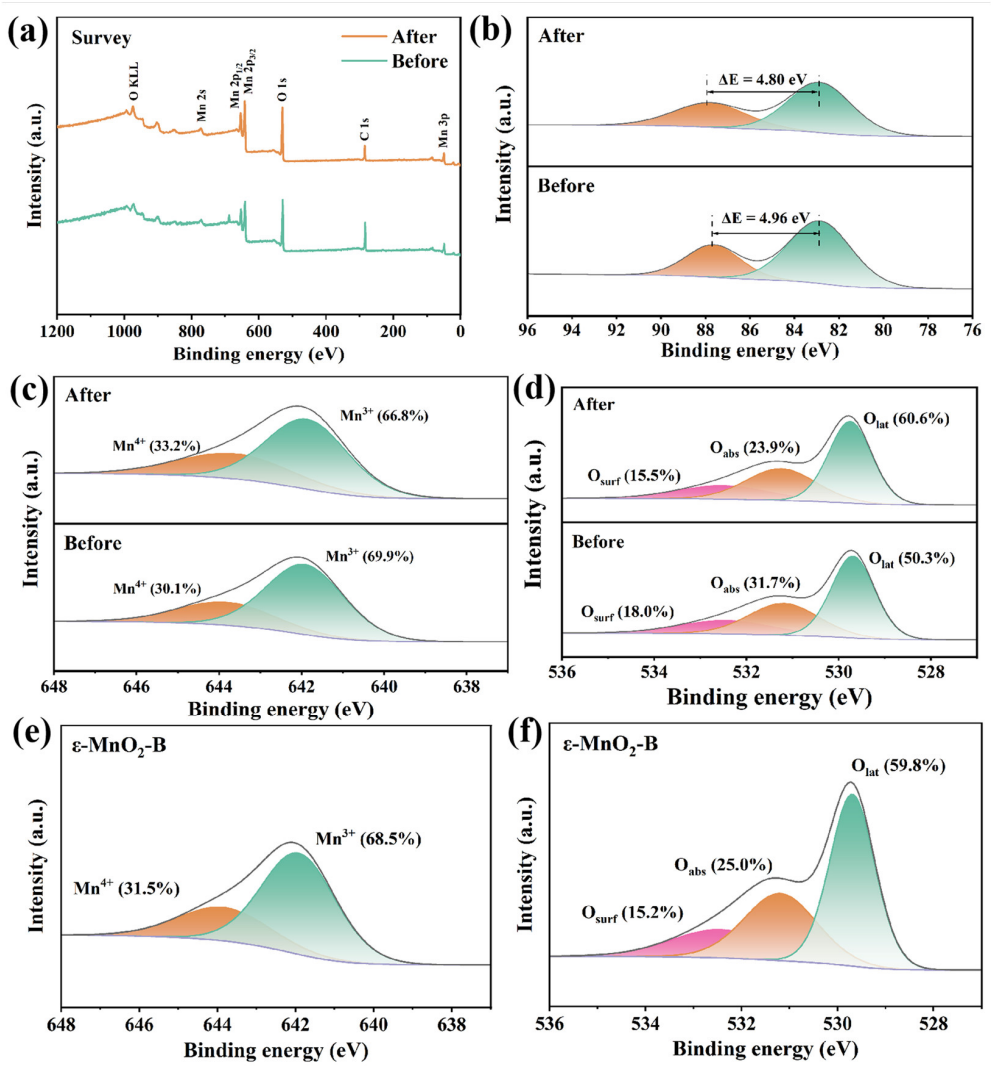

Figure 4. XPS spectra of ε-MnO_2-P: (**a**) survey (full spectrum), (**b**) Mn 3s, (**c**) Mn 2p, and (**d**) O 1s. XPS spectra of ε-MnO_2-B, (**e**) Mn 2p, (**f**) O 1s.

Commonly, sufficiently charged oxygen vacancies on the material surface can act as Lewis dot sites and be attractive to electrophilic molecules (e.g., O_2 and H_2O_2), facilitating the charge transfer process. The O-O bonds in PMS are much weaker than those in both O_2 and H_2O_2, so the PMS molecules adsorbed on the ε-MnO_2-P surface are easily activated by electrons induced by oxygen vacancies to produce the required ROS [28]. The O 1s spectra can be fitted to three peaks at 529.7, 531.2 and 532.4 eV, corresponding to lattice oxygen (O_{lat}), adsorbed oxygen (O_{abs}) and surface oxygen (O_{surf}), respectively. Among them, O_{abs} is generally considered to be a parameter that can indirectly represent the oxygen vacancy concentration [32]. As shown in Figure 4d, the percentage of oxygen vacancies decreased from 31.7% to 23.9% after the reaction, indicating that approximately 7.8% of oxygen vacancies were involved in the degradation of CIP. In contrast, the XPS results of Mn 2p and O 1s for ε-MnO_2-B (Figure 4e,f) indicate that the initial ε-MnO_2-B has a lower low-valent Mn content and smaller ratio of oxygen vacancies than ε-MnO_2-P, which can be responsible for the lower CIP removal efficiency in previous experiments.

To investigate which ROS contributed to the removal of CIP, EPR was used to characterize the ε-MnO_2-P/PMS oxidation system, as shown in Figure 5a,b. After adding DMPO (5,5-dimethyl-1-pyrroline N-oxide) and TEMP (2,2,6,6-tetramethylpiperidine) to capture, ·OH, $SO_4^{\cdot-}$ and $^1O_2$, DMPO-OH/$SO_4^{\cdot-}$ and TEMP-$^1O_2$ were obtained, whose signals could be collected to form the characteristic spectra. There are seven peaks (1:2:1:2:1:2:1)

belonging to DMPOX (5,5-dimethylpyrroline-(2)-oxyl-(1)), the oxidation of DMPO [33]. It should be pointed out that the presence of DMPOX does not indicate that ·OH and $SO_4^{\cdot-}$ did not exist in the system. In contrast, DMPOX is formed because the rate of radicals captured by DMPO is lower than that of oxidation by radicals [34]. Moreover, the short and unstable half-life of DMPO-$SO_4^{\cdot-}$ is easily converted to DMPOX, and thus the signal belonging to DMPOX will be reflected in the EPR result [23,35]. Moreover, three peaks for $^1O_2$ (1:1:1) were clearly visible after the addition of TEMP, confirming the presence of $^1O_2$. The appearance of $^1O_2$ can effectively avoid the generation of byproducts caused by the combination of ·OH and $SO_4^{\cdot-}$ with anions in water (such as Cl^-), which reduces the oxidizability of the system and may increase the toxicity.

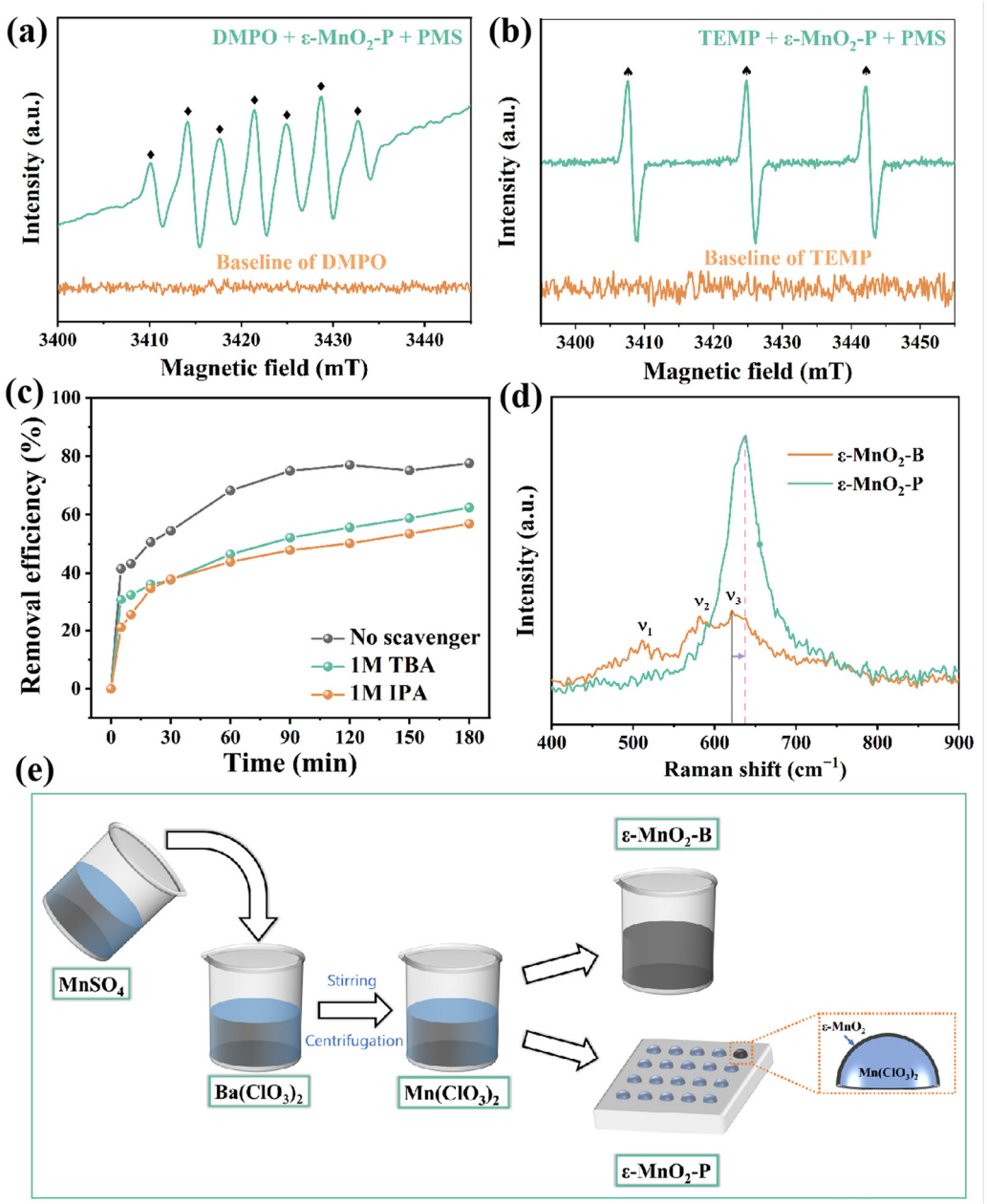

Figure 5. EPR spectra of ε-MnO_2-P in the presence of different trapping agents: (**a**) DMPO and (**b**) TEMP. (**c**) Plots of CIP removal efficiency after the addition of different trapping agents. (**d**) Raman spectra of ε-MnO_2-P and ε-MnO_2-B. (**e**) Schematic diagram of the preparation process of ε-MnO_2-B and ε-MnO_2-P.

Furthermore, quenching experiments were carried out to confirm the contribution of different ROS to the reaction. It is known that the addition of excess isopropanol (IPA, for ·OH and $SO_4^{\cdot-}$, $k_{\cdot OH}$ = 2.8 × 10^9, $k_{SO4^{\cdot-}}$ = 8.3 × 10^7) and tert-butanol (TBA, $k_{\cdot OH}$ = (3.8–7.6) × 10^8, $k_{SO4^{\cdot-}}$ = (4.0–9.1) × 10^5) can consume ·OH and $SO_4^{\cdot-}$ [36]. The removal efficiency of CIP after adding IPA is a bit lower than that after adding TBA, probably because both ·OH and $SO_4^{\cdot-}$ were captured by IPA, while only ·OH was captured by TBA. In addition, it can be observed from the magnitude of decrement that the CIP removal efficiency with IPA only decreased by 5.4% compared to the capture effect with TBA, indicating that ·OH contributed more to the reaction than $SO_4^{\cdot-}$. However, after trapping two free radicals, the removal efficiency of CIP can still be maintained at ~60%, indirectly indicating that $^1O_2$ also plays a notable role in the reaction and is one of the main ROS.

The content difference of oxygen vacancies in ε-MnO_2-B and ε-MnO_2-P can be further confirmed by Raman spectroscopy. As shown in Figure 5d, three main peaks can be observed at 512 cm^{-1} (subsequently referred to as ν_1), 581 cm^{-1} (ν_2) and 620 cm^{-1} (ν_3). Therein, ν_1 represents the metal–oxygen chain of Mn-O-Mn in the octahedral lattice of MnO_2, ν_2 represents the Mn-O stretching vibration in the manganese oxide lattice, and ν_3 represents the Mn-O in the [MnO_6] group of the symmetric stretching vibration. It can be clearly seen that ν_3 of ε-MnO_2-P shows a blueshift compared to ε-MnO_2-B (marked by the pink dashed line), indicating that the Mn-O vibration in the MnO_2 lattice is enhanced in virtue of lattice distortion induced by the introduction of oxygen vacancies. Based on the above results, the microcavity space designed by changing the synthetic interface can introduce more oxygen vacancies for ε-MnO_2-P, thus promoting the degradation of organic pollutants by Fenton-like reactions.

Taken together, the conclusions regarding the influencing factors of SR-AOPs for the removal of CIP have been discussed and validated. Since the catalytic activity of the two ε-MnO_2 materials differs considerably, the preparation process of the material is shown to explain the synthesis mechanism. As shown in Figure 5e, when $Mn(ClO_3)_2$ solution was added to the hydrophobic PTFE plate in the form of liquid droplets, as drying proceeded, the surface of the droplet and the air contact preferentially decomposed to produce a MnO_2 barrier layer. The decomposition process proceeded according to the equation $Mn(ClO_3)_2 \rightarrow MnO_2 + 2ClO_2\uparrow$. With continuous drying, a microcavity anoxic space was generated inside the isolation layer; ultimately, the oxygen vacancies in the prepared ε-MnO_2-P increased, resulting in high catalytic activity. According to the abovementioned results, we hypothesized the mechanism of ε-MnO_2-P removing CIP, and the diagram is shown in Figure 6. First, Mn^{3+} and Mn^{4+} formed a unique redox cycle, and the electron transfer generated during the cycling process promoted the conversion of HSO_5^- to ·OH, $SO_4^{\cdot-}$ and $SO_5^{\cdot-}$ through Equations (1)–(3). Of these, $SO_5^{\cdot-}$ was only produced when high-valent manganese reacts with HSO_5^-, which is one of the reasons why ε-MnO_2-P with a higher proportion of low-valent manganese exhibits a better removal effect. In addition, $SO_4^{\cdot-}$ also reacted with water to form ·OH via a free radical chain reaction, which revealed a slight effect on the overall pH range of the reaction [37]. Meanwhile, $^1O_2$ was produced through the interaction of ·OH and ·OH, or the combination of HSO_5^- with SO_5^{2-} (another form of PMS) [19,38].

$$Mn^{3+} + HSO_5^- \rightarrow Mn^{4+} + SO_4\cdot^- + OH^- \quad (1)$$

$$Mn^{3+} + HSO_5^- \rightarrow Mn^{4+} + SO_4^{2-} + \cdot OH \quad (2)$$

$$Mn^{4+} + HSO_5^- \rightarrow Mn^{3+} + SO_5\cdot^- + H^+ \quad (3)$$

$$SO_4\cdot^- + H_2O \rightarrow \cdot OH + SO_4^{2-} \quad (4)$$

$$HSO_5^- + SO_5^{2-} \rightarrow {}^1O_2 + SO_4^{2-} + HSO_4^- \quad (5)$$

$$Mn^{4+} + S_2O_8^{2-} \rightarrow S_2O_8^{\cdot -} + Mn^{3+} \quad (6)$$

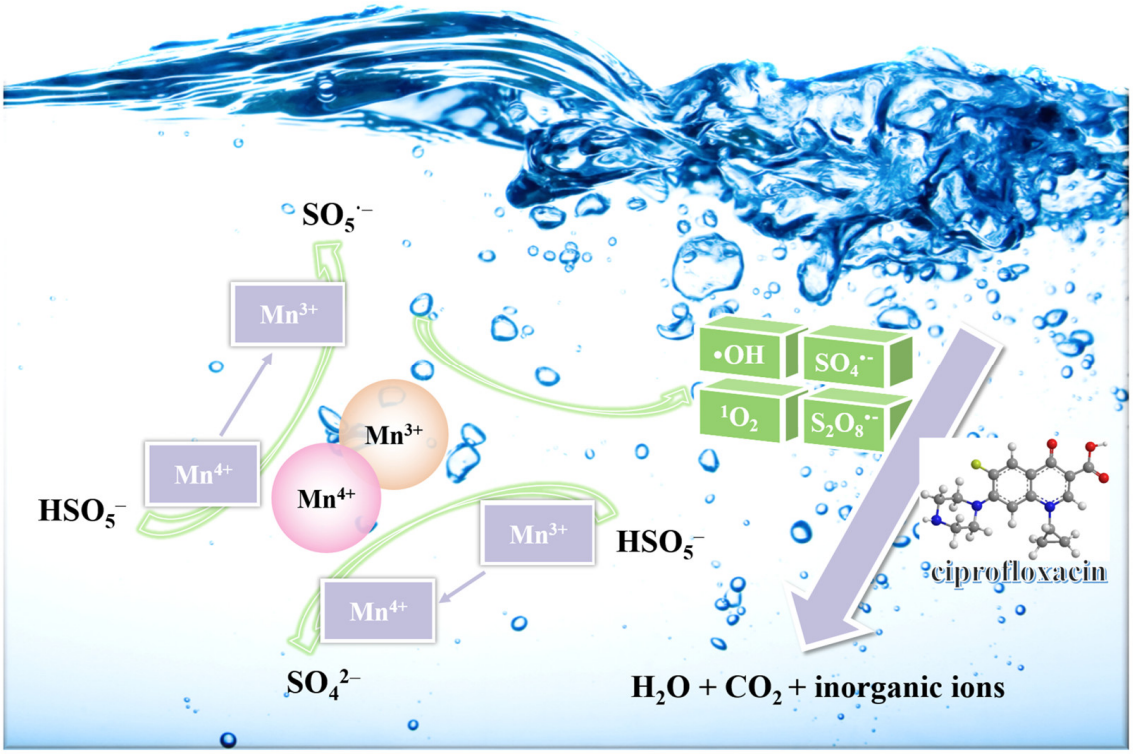

Figure 6. Schematic diagram of the mechanism of CIP degradation by the ε-MnO_2-P/PMS system.

4. Conclusions

In summary, a new route for the preparation of ε-MnO_2-P using a special interface was proposed to improve its catalytic performance as a Fenton-like catalyst. The content of oxygen vacancies in ε-MnO_2-P was regulated by the innovative construction of a microanoxic space to improve its catalytic activity by activating PMS. The ε-MnO_2-P obtained by drying on a hydrophobic surface exhibited the characteristics of low crystallinity, large specific surface area and high Mn^{3+} ratio. The ε-MnO_2-P/PMS oxidation system could achieve rapid degradation of CIP in water under a wide pH range, and ε-MnO_2-P acting as a catalyst exhibited good reusability. EPR and quenching experiments confirmed that ·OH, $SO_4^{\cdot -}$ and $^1O_2$ were the main ROS affecting the reaction, of which $^1O_2$ contributed more. This synthesis method provides a strategy for the preparation of other O-vacancy-rich materials and promotes the development of Fenton-like reactions for wastewater treatment.

Author Contributions: Y.C. (Yulong Chen): conceptualization, methodology, writing—reviewing and editing; Y.C. (Yuan Chi): investigation, data curation, and writing—original draft; X.W.: investigation, writing—reviewing and editing; C.L.: validation; T.L.: formal analysis; M.G.: investigation; C.Z.: resources; B.S.: supervision, investigation. All authors have read and agreed to the published version of the manuscript.

Funding: The authors appreciate the support of the National Natural Science Foundation of China (No. 52072075, 52102126 and 12104093), the Natural Science Foundation of Fujian Province (No. 2021J05122, 2021J05123, 2022J01087, 2022J01552, 2023J01259), the undergraduate education teaching research project of Fujian Province (No. FBJY20230036) and the Qishan Scholar Financial Support from Fuzhou University (GXRC-20099).

Data Availability Statement: All data are contained within the article.

Conflicts of Interest: The authors declare no conflict of interest.

References

1. Yao, Z.; Jiao, W.; Shao, F.; Song, H.; Zhang, H.; Zhou, Q.; Li, A. Fabrication and characterization of amphiphilic magnetic water purification materials for efficient PPCPs removal. *Chem. Eng. J.* **2019**, *360*, 511–518. [CrossRef]
2. Yang, H.; Wang, W.; Wu, X.; Siddique, M.S.; Su, Z.; Liu, M.; Yu, W. Reducing ROS generation and accelerating the photocatalytic degradation rate of PPCPs at neutral pH by doping Fe-N-C to g-C_3N_4. *Appl. Catal. B* **2022**, *301*, 120790. [CrossRef]
3. Dang, V.D.; Adorna, J.; Annadurai, T.; Bui, T.A.N.; Tran, H.L.; Lin, L.; Doong, R. Indirect Z-scheme nitrogen-doped carbon dot decorated Bi_2MoO_6/g-C_3N_4 photocatalyst for enhanced visible-light-driven degradation of ciprofloxacin. *Chem. Eng. J.* **2021**, *422*, 130103. [CrossRef]
4. Chen, M.; Niu, H.; Niu, C.; Guo, H.; Liang, S.; Yang, Y. Metal-organic framework-derived CuCo/carbon as an efficient magnetic heterogeneous catalyst for persulfate activation and ciprofloxacin degradation. *J. Hazard. Mater.* **2022**, *424*, 127196. [CrossRef] [PubMed]
5. Xu, X.; Ding, X.; Yang, X.; Wang, P.; Li, S.; Lu, Z.; Chen, H. Oxygen vacancy boosted photocatalytic decomposition of ciprofloxacin over Bi_2MoO_6: Oxygen vacancy engineering, biotoxicity evaluation and mechanism study. *J. Hazard. Mater.* **2019**, *364*, 691–699. [CrossRef]
6. Ding, J.; Dai, Z.; Qin, F.; Zhao, H.; Zhao, S.; Chen, R. Z-scheme $BiO_{1-x}Br/Bi_2O_2CO_3$ photocatalyst with rich oxygen vacancy as electron mediator for highly efficient degradation of antibiotics. *Appl. Catal. B* **2017**, *205*, 281–291. [CrossRef]
7. Zhou, Y.; Gao, Y.; Pang, S.; Jiang, J.; Yang, Y.; Ma, J.; Yang, Y.; Duan, J.; Guo, Q. Oxidation of fluoroquinolone antibiotics by peroxymonosulfate without activation: Kinetics, products, and antibacterial deactivation. *Water Res.* **2018**, *145*, 210–219. [CrossRef]
8. Wang, A.; Chen, Z.; Zheng, Z.; Xu, H.; Wang, H.; Hu, K.; Yan, K. Remarkably enhanced sulfate radical-based photo-fenton-like degradation of levofloxacin using the reduced mesoporous MnO@MnO_x microspheres. *Chem. Eng. J.* **2020**, *379*, 122340. [CrossRef]
9. Li, X.; Huang, X.; Xi, S.; Miao, S.; Ding, J.; Cai, W.; Liu, S.; Yang, X.; Yang, H.; Gao, J.; et al. Single cobalt atoms anchored on porous N-doped graphene with dual reaction sites for efficient fenton-like catalysis. *J. Am. Chem. Soc.* **2018**, *140*, 12469–12475. [CrossRef]
10. Ghanbari, F.; Moradi, M. Application of peroxymonosulfate and its activation methods for degradation of environmental organic pollutants: Review. *Chem. Eng. J.* **2017**, *310*, 41–62. [CrossRef]
11. Oh, W.; Dong, Z.; Lim, T. Generation of sulfate radical through heterogeneous catalysis for organic contaminants removal: Current development, challenges and prospects. *Appl. Catal. B* **2016**, *194*, 169–201. [CrossRef]
12. Liu, Y.; Qu, R.; Li, X.; Wei, Y.; Feng, L. A bifunctional β-MnO_2 mesh for expeditious and ambient degradation of dyes in activation of peroxymonosulfate (PMS) and simultaneous oil removal from water. *J. Colloid Interface Sci.* **2020**, *579*, 412–424. [CrossRef] [PubMed]
13. Milh, H.; Yu, X.; Cabooter, D.; Dewil, R. Degradation of ciprofloxacin using UV-based advanced removal processes: Comparison of persulfate-based advanced oxidation and sulfite-based advanced reduction processes. *Sci. Total Environ.* **2021**, *764*, 144510. [CrossRef] [PubMed]
14. Ahn, Y.; Choi, J.; Kim, M.; Kim, M.S.; Lee, D.; Bang, W.H.; Yun, E.; Lee, H.; Lee, J.; Lee, C.; et al. Chloride-mediated enhancement in heat-induced activation of peroxymonosulfate: New reaction pathways for oxidizing radical production. *Environ. Sci. Technol.* **2021**, *55*, 5382–5392. [CrossRef]
15. Wang, X.; Jiang, J.; Ma, Y.; Song, Y.; Li, T.; Dong, S. Tetracycline hydrochloride degradation over manganese cobaltate ($MnCo_2O_4$) modified ultrathin graphitic carbon nitride (g-C_3N_4) nanosheet through the highly efficient activation of peroxymonosulfate under visible light irradiation. *J. Colloid Interface Sci.* **2021**, *600*, 449–462. [CrossRef] [PubMed]
16. Guo, Z.; Li, C.; Gao, M.; Han, X.; Zhang, Y.; Zhang, W.; Li, W. Mn−O covalency governs the intrinsic activity of Co-Mn spinel oxides for boosted peroxymonosulfate activation. *Angew. Chem. Int. Ed.* **2020**, *60*, 274–280. [CrossRef] [PubMed]
17. Hu, P.; Long, M. Cobalt-catalyzed sulfate radical-based advanced oxidation: A review on heterogeneous catalysts and applications. *Appl. Catal. B* **2016**, *181*, 103–117. [CrossRef]
18. Zhang, Q.; He, D.; Li, X.; Feng, W.; Lyu, C.; Zhang, Y. Mechanism and performance of singlet oxygen dominated peroxymonosulfate activation on CoOOH nanoparticles for 2,4-dichlorophenol degradation in water. *J. Hazard. Mater.* **2020**, *384*, 121350. [CrossRef]
19. Huang, J.; Dai, Y.; Singewald, K.; Liu, C.; Saxena, S.; Zhang, H. Effects of MnO_2 of different structures on activation of peroxymonosulfate for bisphenol A degradation under acidic conditions. *Chem. Eng. J.* **2019**, *370*, 906–915. [CrossRef]
20. Tao, P.; Shao, M.; Song, C.; Li, C.; Yin, Y.; Wu, S.; Cheng, M.; Cui, Z. Morphologically controlled synthesis of porous Mn_2O_3 microspheres and their catalytic applications on the degradation of methylene blue. *Desalin. Water Treat.* **2015**, *57*, 7079–7084. [CrossRef]
21. Wang, F.; Xiao, M.; Ma, X.; Wu, S.; Ge, M.; Yu, X. Insights into the transformations of Mn species for peroxymonosulfate activation by tuning the Mn_3O_4 shapes. *Chem. Eng. J.* **2021**, *404*, 127097. [CrossRef]
22. Lin, M.; Chen, Z. A facile one-step synthesized epsilon-MnO_2 nanoflowers for effective removal of lead ions from wastewater. *Chemosphere* **2020**, *250*, 126329. [CrossRef] [PubMed]
23. Nawaz, F.; Cao, H.; Xie, Y.; Xiao, J.; Chen, Y.; Ghazi, Z.A. Selection of active phase of MnO_2 for catalytic ozonation of 4-nitrophenol. *Chemosphere* **2017**, *168*, 1457–1466. [CrossRef]
24. Wang, H.; Yin, F.; Chen, B.; Li, G. Synthesis of an ε-MnO_2/metal–organic-framework composite and its electrocatalysis towards oxygen reduction reaction in an alkaline electrolyte. *J. Mater. Chem. A* **2015**, *3*, 16168–16176. [CrossRef]

25. Zhao, J.; Wang, Y.; Li, N.; Wang, S.; Yu, J.; Li, X. Efficient degradation of ciprofloxacin by magnetic γ-Fe_2O_3-MnO_2 with oxygen vacancy in visible-light/peroxymonosulfate system. *Chemosphere* **2021**, *276*, 130257. [CrossRef] [PubMed]
26. Wu, L.; Zhang, Q.; Hong, J.; Dong, Z.; Wang, J. Degradation of bisphenol A by persulfate activation via oxygen vacancy-rich $CoFe_2O_{4-x}$. *Chemosphere* **2019**, *221*, 412–422. [CrossRef] [PubMed]
27. Wang, A.; Zheng, Z.; Wang, H.; Chen, Y.; Luo, C.; Liang, D.; Hu, B.; Qiu, R.; Yan, K. 3D hierarchical H_2-reduced Mn-doped CeO_2 microflowers assembled from nanotubes as a high-performance Fenton-like photocatalyst for tetracycline antibiotics degradation. *Appl. Catal. B* **2020**, *277*, 119171. [CrossRef]
28. Yu, J.; Zeng, T.; Wang, H.; Zhang, H.; Sun, Y.; Chen, L.; Song, S.; Li, L.; Shi, H. Oxygen-defective MnO_{2-x} rattle-type microspheres mediated singlet oxygen oxidation of organics by peroxymonosulfate activation. *Chem. Eng. J.* **2020**, *394*, 124458. [CrossRef]
29. Hong, W.; Shao, M.; Zhu, T.; Wang, H.; Sun, Y.; Shen, F.; Li, X. To promote ozone catalytic decomposition by fabricating manganese vacancies in ε-MnO_2 catalyst via selective dissolution of Mn-Li precursors. *Appl. Catal. B* **2020**, *274*, 119088. [CrossRef]
30. Xiao, Y.; Huo, W.; Yin, S.; Jiang, D.; Zhang, Y.; Zhang, Z.; Liu, X.; Dong, F.; Wang, J.; Li, G.; et al. One-step hydrothermal synthesis of Cu-doped MnO_2 coated diatomite for degradation of methylene blue in Fenton-like system. *J. Colloid Interface Sci.* **2019**, *556*, 466–475. [CrossRef]
31. Huang, Y.; Tian, X.; Nie, Y.; Yang, C.; Wang, Y. Enhanced peroxymonosulfate activation for phenol degradation over MnO_2 at pH 3.5–9.0 via Cu(II) substitution. *J. Hazard. Mater.* **2018**, *360*, 303–310. [CrossRef] [PubMed]
32. Lim, J.; Yang, Y.; Hoffmann, M.R. Activation of peroxymonosulfate by oxygen vacancies-enriched cobalt-doped black TiO_2 nanotubes for the removal of organic pollutants. *Environ. Sci. Technol.* **2019**, *53*, 6972–6980. [CrossRef] [PubMed]
33. Liu, J.; An, F.; Zhu, C.; Zhou, D. Efficient transformation of DDT with peroxymonosulfate activation by different crystallographic MnO_2. *Sci. Total Environ.* **2021**, *759*, 142864. [CrossRef]
34. Xie, M.; Tang, J.; Kong, L.; Lu, W.; Natarajan, V.; Zhu, F.; Zhan, J. Cobalt doped g-C_3N_4 activation of peroxymonosulfate for monochlorophenols degradation. *Chem. Eng. J.* **2019**, *360*, 1213–1222. [CrossRef]
35. Du, J.; Bao, J.; Liu, Y.; Kim, S.H.; Dionysiou, D.D. Facile preparation of porous Mn/Fe_3O_4 cubes as peroxymonosulfate activating catalyst for effective bisphenol A degradation. *Chem. Eng. J.* **2019**, *376*, 119193. [CrossRef]
36. Wang, L.; Lan, X.; Peng, W.; Wang, Z. Uncertainty and misinterpretation over identification, quantification and transformation of reactive species generated in catalytic oxidation processes: A review. *J. Hazard. Mater.* **2021**, *408*, 124436. [CrossRef]
37. Pan, F.; Ji, H.; Du, P.; Huang, T.; Wang, C.; Liu, W. Insights into catalytic activation of peroxymonosulfate for carbamazepine degradation by MnO_2 nanoparticles in-situ anchored titanate nanotubes: Mechanism, ecotoxicity and DFT study. *J. Hazard. Mater.* **2021**, *402*, 123779. [CrossRef]
38. Liu, Y.; Guo, H.; Zhang, Y.; Cheng, X.; Zhou, P.; Wang, J.; Li, W. Fe@C carbonized resin for peroxymonosulfate activation and bisphenol S degradation. *Environ. Pollut.* **2019**, *252*, 1042–1050. [CrossRef]